

# Strong and weak dynamo regimes in Taylor-Couette flows

Ashish Mishra,<sup>1,2,\*</sup> George Mamatsashvili,<sup>1,3</sup> and Frank Stefani<sup>1</sup>

<sup>1</sup>*Helmholtz-Zentrum Dresden-Rossendorf, Bautzner Landstr. 400, D-01328 Dresden, Germany*

<sup>2</sup>*Center for Astronomy and Astrophysics, TU Berlin, Hardenbergstr. 36, 10623 Berlin, Germany*

<sup>3</sup>*Abastumani Astrophysical Observatory, Abastumani 0301, Georgia*

(Dated: January 22, 2025)

We reveal a nonlinear magnetic dynamo in a Taylor-Couette flow at small magnetic Prandtl numbers  $Pm \leq 1$ , which has been previously believed to exist only at higher  $Pm \gtrsim 10$  in this flow. Both the amplitude of initial perturbations and  $Pm$  play a critical role in its onset and evolution. It is shown that this dynamo exists in two main states – a weak state dominated by large-scale modes and a strong, more turbulent state with higher amplitude dominated by small-scale modes. These findings can be important for dynamo processes in many astrophysical settings with small  $Pm$ .

Taylor-Couette (TC) flow is a main setup to experimentally realize and study central hydrodynamical and magnetohydrodynamical (MHD) processes in the laboratory that take place in astrophysical disks. By adjusting the rotation of the cylinders, one can approximately match the rotation profile of the fluid between the cylinders to the Keplerian rotation  $\Omega \propto r^{-3/2}$  of the disks. One of the most important applications of MHD TC flow using liquid metal as a working fluid and subject to an imposed magnetic field is in the theoretical and experimental studies of different – standard [1–9], helical [10–17] and azimuthal [18–20] – flavors of magnetorotational instability (MRI), which is a central process driving angular momentum transport and mass accretion in the disks (see reviews [21–23]).

MRI is closely interlaced with magnetic dynamo, leading to the concept of the nonlinear MRI-dynamo – an important class of instability-driven processes of generation, amplification and sustenance of a large-scale magnetic field, which, in turn, reinforces that instability [24]. The MRI-dynamo has been actively studied mainly in the local shearing-box model of the disks, which allowed to clarify its onset criterion, underlying sustenance dynamics and dependence on fluid viscosity ( $\nu$ ) and magnetic diffusivity ( $\eta$ ) [25–34]. In particular, it was shown that this dynamo is most sensitive to the magnetic Prandtl number  $Pm = \nu/\eta$ , being sustained at  $Pm \gtrsim Pm_c$  and non-existent at  $Pm \lesssim Pm_c$ , where the threshold  $Pm_c$  is generally close to unity,  $Pm_c \sim 1$ , but its specific value depends on the system parameters, such as box size and aspect ratio, shear of a base flow, etc.

In parallel with the local, there have been global studies of the magnetic dynamo action in TC flows to understand mechanisms of magnetic field generation and amplification in real disks beyond the local analysis. Early simulations considered TC flows hydrodynamically unstable according to Rayleigh’s centrifugal criterion and showed that the efficiency of the dynamo in those flows depends on the flow structure (Taylor vortices) resulting from the hydrodynamic instability, specifically on

the interplay between axial and radial velocity components [35–39]. Distinct from this, Guseva et al. [40] considered quasi-Keplerian TC flows similar to disk flows and revealed a sustained subcritical dynamo action there only at high enough  $Pm \gtrsim 10$  and Reynolds numbers  $Re \sim 10^4$ . Since quasi-Keplerian flow is itself hydrodynamically Rayleigh-stable linearly and also nonlinearly [41–44], it is not able to yield a standard kinematic dynamo where very small (seed) initial perturbations of a magnetic field grow exponentially. The dynamo action found in [40] represents instead a complex type of nonlinear, or finite-amplitude dynamo, which, in contrast to the kinematic one, is excited at sufficiently strong initial magnetic field perturbations and relies on MRI that energetically supplies it. As a result, the flow settles down into MHD turbulence with an associated large-scale magnetic field, which mutually sustain each other via interplay of MRI and nonlinear feedback. This dynamo is neither purely large- nor small-scale but involves a broad range of wavelengths. Another type of a dynamo process in a quasi-Keplerian TC flow based on the Taylor instability was identified at sufficiently high  $Rm$  in [45].

In this Letter, we report a nonlinear dynamo action persisting at small  $Pm \leq 1$  in a Rayleigh-stable quasi-Keplerian TC flow. Importantly, we demonstrate that, depending on the amplitude of initial perturbations and  $Pm$  (at fixed  $Re$ ), this dynamo exists in the weak and strong states and characterize their properties.

We consider an infinitely long TC setup consisting of inner and outer cylinders with radii  $r_{in}$  and  $r_{out} = 2r_{in}$  rotating with angular velocities  $\Omega_{in}$  and  $\Omega_{out}$ , respectively, in the cylindrical coordinate system  $(r, \phi, z)$ . The rotation ratio of the cylinders is fixed to  $\Omega_{out}/\Omega_{in} = 0.35$  yielding the Rayleigh-stable quasi-Keplerian rotation profile of the fluid between the cylinders [21], where dynamical processes should therefore be of MHD nature. The cylinders’ height  $L_z$  is such that to give the aspect ratio  $L_z/r_{in} = 10$ . The non-ideal MHD equations for an incompressible fluid are

$$\frac{\partial \mathbf{u}}{\partial t} + (\mathbf{u} \cdot \nabla) \mathbf{u} = -\frac{1}{\rho} \nabla p + \frac{(\nabla \times \mathbf{B}) \times \mathbf{B}}{\mu_0 \rho} + \nu \nabla^2 \mathbf{u}, \quad (1)$$

\* a.mishra@hzdr.de

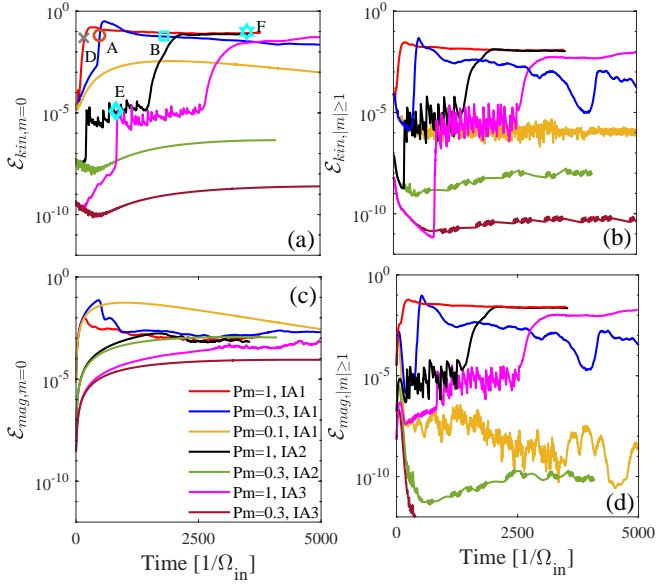


FIG. 1. Evolution of the volume-averaged kinetic  $\mathcal{E}_{kin}$  (top) and magnetic  $\mathcal{E}_{mag}$  (bottom) energies for (a,c) axisymmetric  $m = 0$  and (b,d) non-axisymmetric  $|m| \geq 1$  modes for different initial amplitudes (IAs) and  $Pm \in \{0.1, 0.3, 1\}$ .

$$\frac{\partial \mathbf{B}}{\partial t} = \nabla \times (\mathbf{u} \times \mathbf{B}) + \eta \nabla^2 \mathbf{B}, \quad (2)$$

$$\nabla \cdot \mathbf{u} = 0, \quad \nabla \cdot \mathbf{B} = 0. \quad (3)$$

where  $\rho$  is the constant density,  $\mathbf{u}$  is the velocity,  $p$  is the thermal pressure and  $\mathbf{B}$  is the magnetic field. We normalize length by  $r_{in}$ , time by  $\Omega_{in}^{-1}$ ,  $\mathbf{u}$  by  $\Omega_{in} r_{in}$ ,  $p$  by  $\rho r_{in}^2 \Omega_{in}^2$  and  $\mathbf{B}$  by  $\Omega_{in} r_{in} \sqrt{\rho \mu_0}$ . The main non-dimensional parameters are the Reynolds,  $Re = \Omega_{in} r_{in}^2 / \nu$ , magnetic Reynolds,  $Rm = \Omega_{in} r_{in}^2 / \eta$ , and magnetic Prandtl,  $Pm = Rm / Re$ , numbers.

To solve Eqs. (1)-(3), we use the pseudo-spectral code described in [40]. It employs a high-order finite-difference method along the radial  $r$ -direction and Fourier expansions in the azimuthal  $\phi$ - and axial  $z$ -directions. We take  $N_r = 640$  radial points and  $N_z = 640$  Fourier modes in the axial direction, providing high enough resolution. The total number,  $N_\phi$ , of axisymmetric  $m = 0$  and non-axisymmetric  $|m| \geq 1$  modes, where  $m$  is the azimuthal wavenumber, is set to  $|m| \leq N_\phi = 32$ . No-slip and insulating boundary conditions are adopted for the velocity and magnetic field, respectively. Here we fix  $Re = 10^5$ , which is an order of magnitude higher than that used in a related work by Guseva et al. [40]. We did a resolution test and code validation for such  $Re$  in our recent papers [8, 9].

We impose random initial perturbations with different amplitudes on top of the base TC flow. Figure 1 shows the evolution of the volume-averaged non-dimensional kinetic,  $\mathcal{E}_{kin} = \mathbf{u}^2 / 2$  (the base flow subtracted), and magnetic,  $\mathcal{E}_{mag} = \mathbf{B}^2 / 2$ , energies of axisymmetric and non-axisymmetric modes at three different initial amplitudes

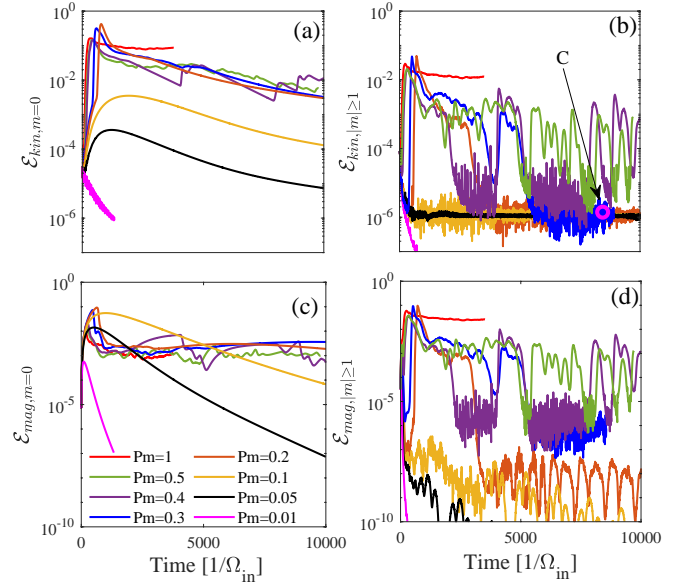


FIG. 2. Same as in Fig. 1 but only for the highest initial amplitude IA1 and a broader range of  $Pm \in \{0.01, 0.05, 0.1, 0.2, 0.3, 0.4, 0.5, 1\}$ . The structure of the weak dynamo state at time moment C in (b) is depicted in Fig. 3.

(IA), IA3 < IA2 < IA1, of velocity and magnetic field perturbations and  $Pm \in \{0.1, 0.3, 1\}$ . Points A, B, D, E and F in Fig. 1(a) denote the key stages of the dynamo evolution (see below) with the corresponding spatial structures of the azimuthal field  $B_\phi$  shown in Fig. 3. Depending on IA and  $Pm$ , different temporal behavior of the energies and hence dynamo regimes are observed. For  $Pm = 1$  and the highest IA1, the magnetic and kinetic energies initially exponentially increase in time (point D) due to MRI and directly reach a saturated quasi-steady state (point F), while at smaller IA2 and IA3 they first reach an intermediate state with about the same low energy level (point E), which lasts for some time, and afterwards grow again, saturating finally at the high level similar to that for IA1. In this high energy state, axisymmetric and non-axisymmetric mode energies are comparable to each other and vary smoothly in time. On the other hand, in the low energy state, only axisymmetric mode energies vary smoothly while those of non-axisymmetric modes rapidly fluctuate and have much smaller amplitude than that of the axisymmetric ones. Thus, for all IAs at  $Pm = 1$ , the system finally arrives the high energy state, referred to as the *strong* dynamo state, the quicker the larger IA is, going in the meantime through a low energy state at smaller IA, referred to as the *weak* dynamo state. At smaller  $Pm = 0.3$ , the strong dynamo state occurs only at the highest IA1 (point B), which sets in directly after the rapid growth phase (point A) without residing temporarily in the weak state. By contrast, at smaller IA3 and IA2, the energies of axisymmetric modes initially grow and then decay very slowly, while those of non-axisymmetric modes decrease and eventually set-

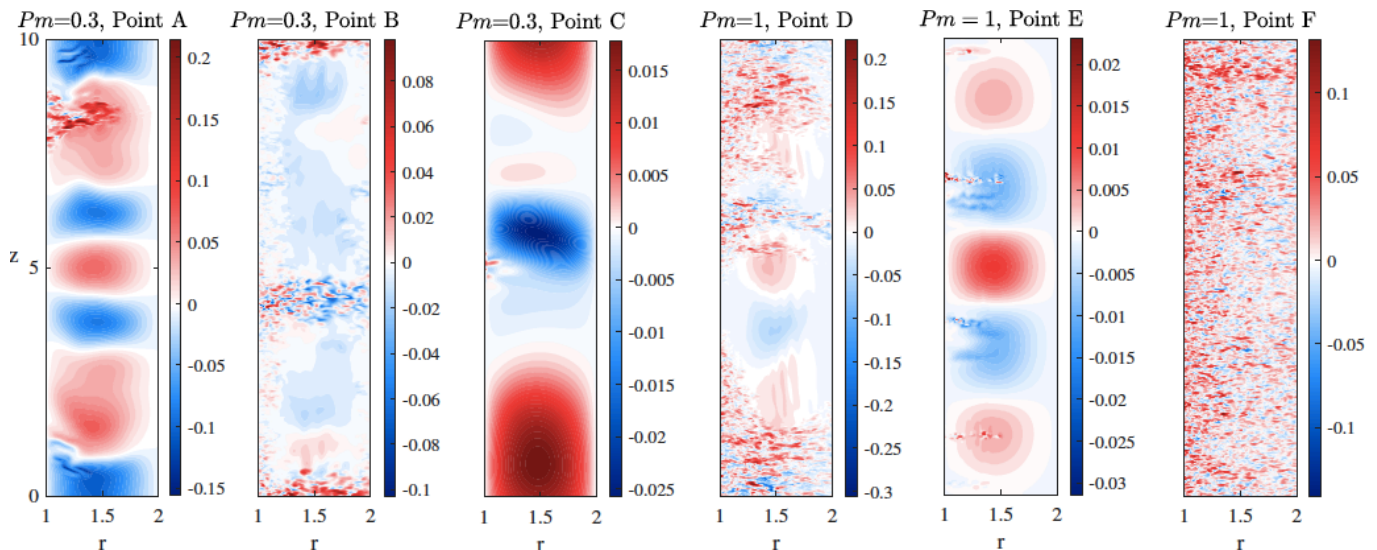


FIG. 3. Structure of the azimuthal field  $B_\phi$  in the  $(r, z)$ -plane at the characteristic time moments corresponding to the points A, B, C at  $Pm = 0.3$  and points D, E, F at  $Pm = 1$  in Figs. 1 and 2, which represent different phases and regimes of the dynamo at these  $Pm$ . Namely, the points A and D represent the growth stages, while the points B and F the saturated states in the strong and the points C and E in the weak dynamo regimes.

tle into the very small (noise) level, indicating transition neither to the weak nor strong dynamo states. The same behavior with decaying dynamo action is observed at  $Pm = 0.1$  for smaller IA3 and IA2 (not shown). Note that the saturation level of the kinetic energy of the non-axisymmetric modes for IA3 and IA2 at  $Pm = 1$  matches that for IA1 at  $Pm = 0.1$ , although the magnetic energy later decreases. This similarity may suggest the existence of a lower energy state, which could be a marginal state separating non-dynamo and dynamo regimes.

Figure 2 shows the similar evolution of the energies but for the highest IA1 and a broader range of  $Pm \in \{0.01, 0.05, 0.1, 0.2, 0.3, 0.4, 0.5, 1\}$ . In this case, the weak and strong dynamo states occur for  $Pm \lesssim 0.1$  and  $Pm \gtrsim 0.1$ , respectively. For intermediate  $Pm = \{0.2, 0.3\}$ , the strong dynamo is sustained initially for some time but eventually settles down into the weak state, while for  $Pm = \{0.4, 0.5\}$  it irregularly alternates between the strong and weak states, as clearly seen for non-axisymmetric modes in Figs. 2(b) and 2(d). Note also that the energies of the latter modes never drop below the low-energy state threshold of the weak dynamo. By contrast, a statistically steady strong turbulent dynamo is consistently observed at  $Pm = 1$ .

To further describe these strong and weak dynamo states, in Fig. 3 we plot the structure of  $B_\phi$  in the  $(r, z)$ -plane for the same  $Pm$  and characteristic time moments as marked in Figs. 1 and 2. For  $Pm = 0.3$ , during a rapid growth of the energies towards the strong regime (point A in Fig. 1), the azimuthal field has the form of regular cells, like those in the case of MRI with a constant axial background field [5–7] with the small turbulent spots emerging at the inner cylinder wall. By contrast, in the growth phase at  $Pm = 1$  (point D), a larger

portion of the flow is turbulent, coexisting with the regular cells. In the saturated strong state for  $Pm = 1$  (point F), the flow is fully turbulent dominated by small-scale structures uniformly filling up the entire domain, similar to that reported in [40] but at higher  $Pm = 10$ , whereas for  $Pm = 0.3$  (point B) the flow consists of evenly distributed highly turbulent spots between more regular larger-scale structures. Note that these large-scale cells do not fully fade away, indicating continual competition between them and localized turbulence. On the other hand, in the weak state, the cells are the dominant structures with some smaller and weaker turbulent spots, as seen for  $Pm = 0.3$  at point C (see also Fig. 2) and for  $Pm = 1$  at point E (see also Fig. 1). Comparing these saturated states, we notice that the transition from the weak to strong dynamos with increasing  $Pm$  occurs through the emergence and growth of turbulent spots on the original regular cells of the weak dynamo. These turbulent spots spread and prevail over the cells, filling up the flow domain in the strong dynamo state.

To find the length-scales contained in these two main dynamo states, we did spectral analysis of the energies. Figures 4(a) and 4(b) show the radially and azimuthally integrated, time-averaged kinetic and magnetic energy spectra, respectively, in the weak (dashed curves) and strong (solid curves) quasi-steady states versus the axial wavenumber  $k_z$ . It is seen that the main qualitative distinction between the strong and weak regimes is that in the first one the magnetic energy spectrum spreads over a broad range of  $k_z$ , from the lowest ones,  $2\pi/L_z$ , corresponding to the domain height  $L_z$ , up to the highest resistive ones  $Rm^{1/2}$ , whereas in the second one, it is concentrated mostly at lower  $k_z \lesssim 10$  and is steeper. In the strong state, the spectrum is nearly flat up to

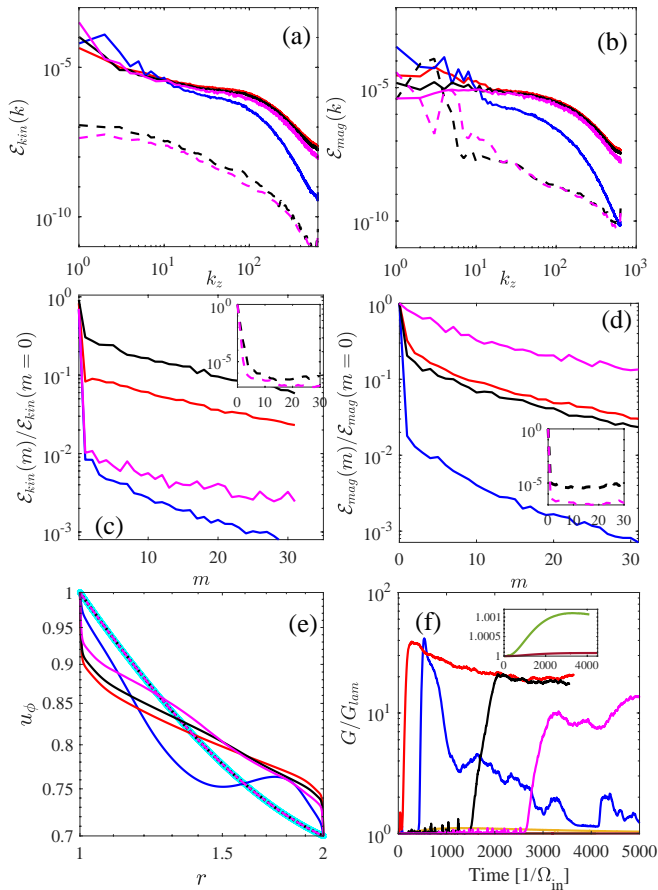


FIG. 4. Kinetic (left) and magnetic (right) energy spectra as a function of (a,b) the axial wavenumber  $k_z$  and (c,d) azimuthal wavenumber  $m$  in the saturated states for the same parameters (colors of the curves) as in Fig. 1. The azimuthal spectra are normalized by the respective energies of the axisymmetric  $m = 0$  modes. Solid and dashed curves correspond to the strong and weak dynamo states, respectively. (e) Radial profile of the azimuthal velocity  $u_\phi$  established in these saturated states at mid-height with the cyan line representing the classical TC profile. (f) Evolution of the normalized torque  $G/G_{lam}$  at the cylinder walls.

$k_z \sim 100$  for  $Pm = 1$  and all IA and drop steeply with  $k_z$  at  $k_z \gtrsim 100$  due to dissipation (Fig. 4b). Also, it becomes steeper with decreasing  $Pm$ , as for  $Pm = 0.3$  shown in Fig. 4(b) with blue curve. In this state, the kinetic energy spectrum behaves similar to the magnetic one, but is higher at lower  $k_z \lesssim 20$ , having at these  $k_z$  more power at  $Pm = 0.3$  than that at  $Pm = 1$  (Fig. 4a). At intermediate  $20 \lesssim k_z \lesssim 100$ , it is flatter for  $Pm = 1$  than that for  $Pm = 0.3$  and in the dissipation range at  $k_z \gtrsim 100$  it decreases the steeper the smaller  $Pm$  is. The larger aspect ratio  $L_z/r_{in} = 10$  adopted here has allowed us to capture the increase of the kinetic energy at lower  $k_z$ , i.e., emergence of large-scale motions, in contrast to the flatter spectrum at smaller and intermediate  $k_z$ , as also observed for  $Pm = 10$  at lower  $L_z/r_{in} = 1.4$  by Guseva et al. [40]. On the other hand, in the weak dy-

namo state at  $Pm = 1$ , the kinetic energy spectrum is mostly flat at small  $k_z \lesssim 20$  but drops more steeply with increasing  $k_z$  than that in the strong state.

Figures 4(c) and 4(d) show the radially and axially integrated, time-averaged energy spectra as a function of  $m$ . These spectra are normalized by the respective energies of the axisymmetric  $m = 0$  modes in order to bring out the role of these modes relative to non-axisymmetric ones. It is seen that in the strong state, for  $Pm = 1$  and higher IA, the kinetic energy is predominantly contained in  $m = 0$  modes, whereas the relative amplitude of non-axisymmetric modes is higher in the magnetic energy. The axisymmetric modes dominate both the kinetic and magnetic energy spectra in the weak state, there is only a small portion of energy in the  $|m| \geq 1$  modes distributed evenly over  $m$ , and therefore this state is axisymmetric.

Figure 4(e) shows the radial profile of the azimuthal velocity at the mid-height of the cylinder. The flow profile changes significantly during saturation in the strong dynamo regime at  $Pm = 1$ , with larger shear appearing near the cylinder walls. For  $Pm = 0.3$ , the flow profile is mostly modified between the cylinders and the shear is not strong at the boundaries compared to that for  $Pm = 1$ . By contrast, the azimuthal velocity profile is not much changed in the weak state. The angular momentum transport in the TC setup is quantified by the torques exerted on the cylinders [8, 46],

$$G_{in,out} = -\frac{r_{in,out}^3}{Re} \int_0^{2\pi} \int_0^{L_z} \frac{d}{dr} \left( \frac{u_\phi}{r} \right) \Big|_{r=r_{in,out}} d\phi dz, \quad (4)$$

which are equal to each other,  $G_{in} = G_{out} \equiv G$ , in the quasi-steady state. The evolution of the normalized torque  $G/G_{lam}$  is shown in Fig. 4(f), where  $G_{lam} = -(2\pi L_z/Re)r_{in}^3 d(u_\phi/r)/dr|_{r=r_{in}}$  is the torque in the initial laminar state. As expected, the torque evolves similar to the energies in Fig. 1, being higher in the strong dynamo regime. For IA3 and IA2 at  $Pm = 1$ , it initially fluctuates in the weak state for some time and then increases as dynamo transitions to the strong state.

In this Letter, we revealed two distinct – strong and weak – subcritical dynamo regimes in quasi-Keplerian TC flows at low  $Pm \leq 1$ . This basic flow configuration pertaining to astrophysical disks in Keplerian rotation has been previously believed to support *no* dynamo action at such small  $Pm$ . The emergence each of these regimes depends on the initial amplitude of perturbations and  $Pm$ . At lower  $Pm$  and/or the initial amplitude, the flow eventually settles down into the weak state, while at sufficiently high initial amplitude and/or  $Pm$  it undergoes transition into the strong state either directly or after going through the weak state first. These two states have, respectively, high and low magnetic energy and angular momentum transport levels as well as qualitatively different spatial structures. In the strong regime, the flow is fully turbulent dominated by small-scale modes, whereas in the weak regime, large-scale modes with sizes comparable to the flow size prevail accompanied with lo-

calized patches of weak turbulence.

These results can be important for (small-scale) dynamo processes in many astrophysical settings with small  $Pm \lesssim 1$ , such as protoplanetary disks, interiors of solar-like stars or liquid cores of rocky planets, and contribute to understanding of sustained dynamo action therein, which is thought in general problematic to excite at small  $Pm$  [24, 28, 32, 47], so its occurrence in these objects is still not well understood. Specifically, the identified strong and weak dynamo states identified in this Letter and transitions between them, resulting in abrupt changes in the torque (Fig. 4f), can have implications for angular momentum and mass transport variabilities in these objects. Further studies will clarify sustenance mechanism of both these dynamo states and, in partic-

ular, their persistence at small  $Pm$ . As in local shear-ular box models of disk dynamo, which is governed by the interplay between the nonmodal growth of MRI and nonlinear (transverse cascade) feedback [27, 31, 32, 48], we expect that MRI and similar nonlinear processes are at the core of the sustenance of these dynamo states in the considered global TC setup as well. The effects of curvature (i.e., the ratio  $r_{in}/r_{out}$ ), aspect  $L_z/r_{in}$  and the rotation  $\mu$  ratios on the dynamo states will also be explored.

This work received funding from the European Union's Horizon 2020 research and innovation program under the ERC Advanced Grant Agreement No. 787544 and from Shota Rustaveli National Science Foundation of Georgia (SRNSFG) [grant number FR-23-1277]. We thank A. Guseva for providing the pseudo-spectral code.

- 
- [1] H. Ji, J. Goodman, and A. Kageyama, Magnetorotational instability in a rotating liquid metal annulus, *Mon. Not. R. Astron. Soc.* **325**, L1 (2001).
- [2] J. Goodman and H. Ji, Magnetorotational instability of dissipative couette flow, *J. Fluid Mech.* **462**, 365–382 (2002).
- [3] G. Rüdiger and Y. Zhang, MHD instability in differentially-rotating cylindric flows, *Astron. Astrophys.* **378**, 302 (2001).
- [4] X. Wei, H. Ji, J. Goodman, F. Ebrahimi, E. Gilson, F. Jenko, and K. Lackner, Numerical simulations of the Princeton magnetorotational instability experiment with conducting axial boundaries, *Phys. Rev. E* **94**, 063107 (2016).
- [5] H. W. Winarto, H. Ji, J. Goodman, F. Ebrahimi, E. P. Gilson, and Y. Wang, Parameter space mapping of the Princeton magnetorotational instability experiment, *Phys. Rev. E* **102**, 10.1103/PhysRevE.102.023113 (2020).
- [6] A. Mishra, G. Mamatsashvili, and F. Stefani, From helical to standard magnetorotational instability: Predictions for upcoming liquid sodium experiments, *Phys. Rev. Fluids* **7**, 064802 (2022).
- [7] Y. Wang, E. P. Gilson, F. Ebrahimi, J. Goodman, and H. Ji, Observation of axisymmetric standard magnetorotational instability in the laboratory, *Phys. Rev. Lett.* **129**, 115001 (2022).
- [8] A. Mishra, G. Mamatsashvili, and F. Stefani, Nonlinear evolution of magnetorotational instability in a magnetized Taylor-Couette flow: Scaling properties and relation to upcoming DRESHDYN-MRI experiment, *Phys. Rev. Fluids* **8**, 083902 (2023).
- [9] A. Mishra, G. Mamatsashvili, and F. Stefani, Nonaxisymmetric modes of magnetorotational and possible hydrodynamical instabilities in the upcoming dresdyn-mri experiments: Linear and nonlinear dynamics, *Phys. Rev. Fluids* **9**, 033904 (2024).
- [10] R. Hollerbach and G. Rüdiger, New type of magnetorotational instability in cylindrical Taylor-Couette flow, *Phys. Rev. Lett.* **95**, 124501 (2005).
- [11] F. Stefani, T. Gundrum, G. Gerbeth, G. Rüdiger, M. Schultz, J. Szklarski, and R. Hollerbach, Experimental evidence for magnetorotational instability in a Taylor-Couette flow under the influence of a helical magnetic field, *Phys. Rev. Lett.* **97**, 184502 (2006).
- [12] W. Liu, J. Goodman, I. Herron, and H. Ji, Helical magnetorotational instability in magnetized Taylor-Couette flow, *Phys. Rev. E* **74**, 056302 (2006).
- [13] F. Stefani, G. Gerbeth, T. Gundrum, R. Hollerbach, J. Priede, G. Rüdiger, and J. Szklarski, Helical magnetorotational instability in a Taylor-Couette flow with strongly reduced Ekman pumping, *Phys. Rev. E* **80**, 066303 (2009).
- [14] O. N. Kirillov and F. Stefani, On the Relation of Standard and Helical Magnetorotational Instability, *Astrophys. J.* **712**, 52 (2010).
- [15] G. Mamatsashvili and F. Stefani, Linking dissipation-induced instabilities with nonmodal growth: The case of helical magnetorotational instability, *Phys. Rev. E* **94**, 051203 (2016).
- [16] G. Mamatsashvili, F. Stefani, A. Guseva, and M. Avila, Quasi-two-dimensional nonlinear evolution of helical magnetorotational instability in a magnetized Taylor-Couette flow, *New J. Phys.* **20**, 013012 (2018).
- [17] G. Mamatsashvili, F. Stefani, R. Hollerbach, and G. Rüdiger, Two types of axisymmetric helical magnetorotational instability in rotating flows with positive shear, *Phys. Rev. Fluids* **4**, 103905 (2019).
- [18] R. Hollerbach, V. Teeluck, and G. Rüdiger, Nonaxisymmetric magnetorotational instabilities in cylindrical Taylor-Couette flow, *Phys. Rev. Lett.* **104**, 044502 (2010).
- [19] M. Seilmayer, V. Galindo, G. Gerbeth, T. Gundrum, F. Stefani, M. Gellert, G. Rüdiger, M. Schultz, and R. Hollerbach, Experimental evidence for nonaxisymmetric magnetorotational instability in a rotating liquid metal exposed to an azimuthal magnetic field, *Phys. Rev. Lett.* **113**, 024505 (2014).
- [20] A. Mishra, G. Mamatsashvili, V. Galindo, and F. Stefani, Convective, absolute and global azimuthal magnetorotational instabilities, *J. Fluid Mech.* **922**, R4 (2021).
- [21] G. Rüdiger, M. Gellert, R. Hollerbach, M. Schultz, and F. Stefani, Stability and instability of hydromagnetic Taylor-Couette flows, *Phys. Rep.* **741**, 1 (2018).
- [22] H. Ji and J. Goodman, Taylor-Couette flow for as-

- trophysical purposes, *Philos. Trans. R. Soc. A* **381**, 20220119 (2023).
- [23] F. Stefani, Liquid-metal experiments on geophysical and astrophysical phenomena, *Nat. Rev. Phys.* **6**, 409 (2024).
- [24] F. Rincon, Dynamo theories, *J. Plasma Phys.* **85**, 205850401 (2019).
- [25] F. Rincon, G. I. Ogilvie, and M. R. E. Proctor, Self-Sustaining Nonlinear Dynamo Process in Keplerian Shear Flows, *Phys. Rev. Lett.* **98**, 254502 (2007).
- [26] G. Lesur and G. I. Ogilvie, On self-sustained dynamo cycles in accretion discs, *Astron. Astrophys.* **488**, 451 (2008).
- [27] J. Hecault, F. Rincon, C. Cossu, G. Lesur, G. I. Ogilvie, and P. Y. Longaretti, Periodic magnetorotational dynamo action as a prototype of nonlinear magnetic-field generation in shear flows, *Phys. Rev. E* **84**, 036321 (2011).
- [28] A. Riols, F. Rincon, C. Cossu, G. Lesur, G. I. Ogilvie, and P. Y. Longaretti, Dissipative effects on the sustainment of a magnetorotational dynamo in Keplerian shear flow, *Astron. Astrophys.* **575**, A14 (2015).
- [29] J.-M. Shi, J. M. Stone, and C. X. Huang, Saturation of the magnetorotational instability in the unstratified shearing box with zero net flux: convergence in taller boxes, *Mon. Not. R. Astron. Soc.* **456**, 2273 (2016).
- [30] F. Nauman and M. E. Pessah, Sustained Turbulence in Differentially Rotating Magnetized Fluids at a Low Magnetic Prandtl Number, *Astrophys. J.* **833**, 187 (2016).
- [31] A. Riols, F. Rincon, C. Cossu, G. Lesur, G. I. Ogilvie, and P. Y. Longaretti, Magnetorotational dynamo chimeras. The missing link to turbulent accretion disk dynamo models?, *Astron. Astrophys.* **598**, A87 (2017).
- [32] G. Mamatsashvili, G. Chagelishvili, M. E. Pessah, F. Stefani, and G. Bodo, Zero Net Flux MRI Turbulence in Disks: Sustenance Scheme and Magnetic Prandtl Number Dependence, *Astrophys. J.* **904**, 47 (2020).
- [33] L. E. Held and G. Mamatsashvili, MRI turbulence in accretion discs at large magnetic Prandtl numbers, *Mon. Not. R. Astron. Soc.* **517**, 2309 (2022).
- [34] J. Guilet, A. Reboul-Salze, R. Raynaud, M. Bugli, and B. Gallet, MRI-driven dynamo at very high magnetic Prandtl numbers, *Mon. Not. R. Astron. Soc.* **516**, 4346 (2022).
- [35] A. P. Willis and C. F. Barenghi, A Taylor-Couette dynamo, *Astron. Astrophys.* **393**, 339 (2002).
- [36] R. Laguerre, C. Nore, J. Leorat, and J. L. Guermond, Cyclic nonlinear dynamo action in a finite Taylor Couette flow, in *Journal of Physics Conference Series*, Journal of Physics Conference Series, Vol. 137 (IOP, 2008) p. 012019.
- [37] C. Nore, J. L. Guermond, R. Laguerre, J. Léorat, and F. Luddens, Nonlinear dynamo in a short Taylor-Couette setup, *Phys. Fluids* **24**, 094106-094106-15 (2012).
- [38] C. Gissinger, The Taylor-vortex dynamo, *Phys. Fluids* **26**, 044101 (2014).
- [39] F. Marcotte, B. Gallet, F. Pétrélis, and C. Gissinger, Enhanced dynamo growth in nonhomogeneous conducting fluids, *Phys. Rev. E* **104**, 015110 (2021).
- [40] A. Guseva, R. Hollerbach, A. P. Willis, and M. Avila, Dynamo Action in a Quasi-Keplerian Taylor-Couette Flow, *Phys. Rev. Lett.* **119**, 164501 (2017).
- [41] H. Ji, M. Burin, E. Schartman, and J. Goodman, Hydrodynamic turbulence cannot transport angular momentum effectively in astrophysical disks, *Nat.* **444**, 343 (2006).
- [42] M. Avila, Stability and Angular-Momentum Transport of Fluid Flows between Corotating Cylinders, *Phys. Rev. Lett.* **108**, 124501 (2012).
- [43] J. M. Lopez and M. Avila, Boundary-layer turbulence in experiments on quasi-Keplerian flows, *J. Fluid Mech.* **817**, 21 (2017).
- [44] L. Shi, B. Hof, M. Rampp, and M. Avila, Hydrodynamic turbulence in quasi-Keplerian rotating flows, *Phys. Fluids* **29**, 044107 (2017).
- [45] G. Rüdiger and M. Schultz, Large-scale dynamo action of magnetized Taylor-Couette flows, *Mon. Not. R. Astron. Soc.* **493**, 1249 (2020).
- [46] A. Guseva, A. P. Willis, R. Hollerbach, and M. Avila, Transition to magnetorotational turbulence in Taylor-Couette flow with imposed azimuthal magnetic field, *New J. Phys* **17**, 093018 (2015).
- [47] M. Rempel, T. Bhatia, L. Bellot Rubio, and M. J. Korpilagg, Small-Scale Dynamos: From Idealized Models to Solar and Stellar Applications, *Space Sci. Rev.* **219**, 36 (2023).
- [48] D. Gogichaishvili, G. Mamatsashvili, W. Horton, G. Chagelishvili, and G. Bodo, Nonlinear Transverse Cascade and Sustenance of MRI Turbulence in Keplerian Disks with an Azimuthal Magnetic Field, *Astrophys. J.* **845**, 70 (2017).